Journal of Power Sources 195 (2010) 7587–7593

Contents lists available at ScienceDirect

Journal of Power Sources

journal homepage: www.elsevier.com/locate/jpowsour

# Advanced ceramic interconnect material for solid oxide fuel cells: Electrical and thermal properties of calcium- and nickel-doped yttrium chromites

Kyung Joong Yoon*, Carolyn N. Cramer, Jeffry W. Stevenson, Olga A. Marina

*Pacific Northwest National Laboratory, Richland, WA 99354, USA*

ARTICLE INFO

*Article history:*
Received 14 May 2010
Received in revised form 10 June 2010
Accepted 11 June 2010
Available online 22 June 2010

*Keywords:*
Doped yttrium chromite
Perovskite
Solid oxide fuel cell
Ceramic interconnect
Conductivity
Sinterability

ABSTRACT

The structural, thermal and electrical characteristics of calcium- and nickel-doped yttrium chromites were studied for potential use as the interconnect material in high temperature solid oxide fuel cells (SOFCs) and other high temperature electrochemical and thermoelectric devices. The $Y_{0.8}Ca_{0.2}Cr_{1-x}Ni_xO_{3\pm\delta}$ compositions with $x = 0$–$0.15$ showed single phase orthorhombic perovskite structures between 25 and 1200 °C over a wide range of oxygen partial pressures. Nickel doping remarkably enhanced sintering behavior of otherwise refractory chromites, and densities 94% of theoretical density were obtained after sintering at 1400 °C in air with 15 at.% Ni. The thermal expansion coefficient (TEC) was increased with nickel content to closely match that of an 8 mol% yttria-stabilized zirconia (YSZ) electrolyte for $0.05 \leq x \leq 0.15$. Nickel doping significantly improved the electrical conductivity in both oxidizing and reducing atmospheres. Undesirable oxygen ion "leakage" current was insignificant in dual atmosphere conditions. No interfacial interactions with YSZ were detected after firing at 1400 °C.

Published by Elsevier B.V.

## 1. Introduction

Solid oxide fuel cell (SOFC) represents one of the environmentally clean and versatile means of efficiently generating electrical power utilizing various fuel sources. In SOFC stacks, multiple cells are electrically connected in series via interconnects to accumulate the output voltage, and one of the recognized materials-related challenges in the SOFC technology is the development of interconnect materials. Since the interconnect is exposed to a large oxygen partial pressure gradient and makes electrical connection between cells, there are rigorous requirements in the material's properties such as chemical and dimensional stability, high electronic conductivity and negligible ionic conductivity in oxidizing and reducing atmospheres, good sinterability, thermal expansion match and chemical compatibility with other cell components.

Currently, there are two major approaches in developing interconnect materials: metallic and ceramic [1,2]. The major advantages of metallic interconnect are high electronic and thermal conductivities, low cost, and ease of manufacturing [3,4]. However, the operating temperature of the SOFC with the metallic interconnect is limited to ~800 °C or below to prevent an excessive chromium oxide scale growth and cathode poisoning [5–9]. Certain SOFC stack designs which offer their own practical merits at high temperature operation require ceramic interconnects despite their lower electrical conductivity and higher materials cost compared to the metallic interconnects. Currently, acceptor-doped lanthanum chromite is the state-of-the-art ceramic interconnect material [10–13]. It is electrically conductive and chemically stable in wide oxygen partial pressure range, and thermal expansion can be matched with yttria-stabilized zirconia (YSZ) electrolyte by adjusting A-site- and B-site doping [10,14–18]. The major challenge for lanthanum chromite-based materials for SOFC interconnect applications is their extremely inferior sintering behavior in air which has been attributed to the development of a thin layer of $Cr_2O_3$ at the interparticle necks during the initial stages of sintering [1,19]. In addition, lanthanum chromite can react with the YSZ electrolyte at high temperatures causing the formation of a highly resistive lanthanum zirconate ($La_2Zr_2O_7$) phase [20], which makes cost-effective co-firing processes impractical. Therefore, developments of an advanced interconnect material with high electrical conductivity and stability in dual atmospheres, improved sinterability in air, and chemical compatibility with YSZ would be extremely advantageous.

Acceptor-doped yttrium chromite is considered to be one of the promising alternatives to acceptor-doped lanthanum chromite because it is more stable with respect to the formation of hydroxides in SOFC operating conditions, and the formation of impurity phases can be effectively avoided at co-firing temperatures (~1400 °C) [21,22]. In addition, calcium-doped yttrium

* Corresponding author at: Pacific Northwest National Laboratory, Energy & Environmental Directorate, 902 Battelle Blvd, Richland, WA 99354, USA.
Tel.: +1 509 372 4255; fax: +1 509 375 2186.
*E-mail addresses:* kyungjoong.yoon@pnl.gov, kyungjoong.yoon@gmail.com (K.J. Yoon).

0378-7753/$ – see front matter. Published by Elsevier B.V.
doi:10.1016/j.jpowsour.2010.06.040

chromite exhibits higher mechanical strength than lanthanum chromite-based materials [23]. Researchers have studied thermal and electrical properties of doped and undoped yttrium chromite [21,22,24–26], and the major drawback of yttrium chromite is considered to be its lower electrical conductivity than lanthanum chromite [2]. Improved properties can possibly be obtained through doping yttrium chromite with iso- and/or heterovalent cations. In this work, calcium- and nickel-doped yttrium chromites were synthesized using the glycine nitrate method. The effect of nickel doping on chemical stability, sintering and thermal expansion behavior, microstructure, electronic and ionic conductivity, and chemical compatibility with YSZ (i.e. the properties essential for the SOFC interconnect application) was studied. Details of the study on electrical conductivity and dimensional stability, including a defect model, are reported separately [27].

## 2. Experimental

The compositions of $Y_{0.8}Ca_{0.2}Cr_{1-x}Ni_xO_{3\pm\delta}$ ($x$ = 0–0.3) were synthesized using the glycine nitrate process [28]. The precursors of yttrium, calcium, chromium, and nickel nitrates were standardized by gravimetric analysis, and mixed according to the desired stoichiometry with glycine. The glycine/nitrate mixtures were combusted, and the raw powders were calcined at 1200 °C for 2 h in air. After calcination, the phase purity was verified using X-ray diffraction (XRD) analysis (Philips 3100 XRG, Philips Analytical Inc.). The chemical stability in reducing atmosphere was confirmed by annealing the powders at 800 °C in humidified hydrogen ($pO_2 = 4 \times 10^{-22}$ atm) for 12 h and examined via XRD. The phase stability between 25 and 1200 °C was studied using a Philips X'Pert-MPD X-ray diffractometer with secondary beam graphite monochromated Cu K$\alpha$ radiation, equipped with an Anton Paar HTK1200 high-temperature chamber.

Rectangular specimens were prepared by uniaxial pressing at 35 MPa followed by isostatic pressing at 200 MPa. Sintering shrinkage was measured at temperatures up to 1400 °C in a dilatometer using ~3 mm × ~3 mm × ~14 mm bars, and the sintered samples were used to measure thermal expansion coefficients (TECs) in the temperature range of 100–900 °C in air. Samples for scanning electron microscopy (SEM) analysis (JEOL JSM-7600F equipped with energy dispersive X-ray spectroscopy (EDS) detector) were sintered at 1400 °C for 4 h, polished, and thermally etched at 1375 °C. Grain size was determined using the line intersection method.

Electrical conductivity measurements were performed by a four-probe DC method using ~3 mm × ~3 mm × ~30 mm rectangular bars sintered at 1400–1700 °C for 12 h to achieve the maximum density. The electrical contacts were made using Pt wires and Pt paste, and conductivity was measured in the temperature range 600–900 °C while varying the oxygen partial pressure by mixing oxygen and nitrogen for oxidizing atmospheres ($pO_2$ = 0.001–0.21 atm), and carbon dioxide and forming gas (3% $H_2$ in $N_2$) for reducing atmospheres ($pO_2 = 10^{-17}$–$10^{-11}$ atm).

Oxygen permeation measurements were performed on a ~98% dense $Y_{0.8}Ca_{0.2}Cr_{0.85}Ni_{0.15}O_3$ disc in the temperature range 400–900 °C. The ~2.5 mm thick disc was uniaxially pressed at 35 MPa and isostatically pressed at 200 MPa followed by sintering at 1550 °C. It was mounted between two alumina tubes and sealed with gold o-rings at 900 °C by pressure loading. Forming gas was fed to the permeate side, and air was supplied to the feed side, each at a constant flow rate of 30 $cm^3$ $min^{-1}$. The oxygen partial pressure of the $H_2/N_2$ output gas on the permeate side was measured using a zirconia-based oxygen sensor, and the oxygen flux through the disc was calculated based on the assumption that the increase in the total amount of oxygen in the permeate gas (resulting in increases in the oxygen partial pressure, $\Delta pO_2$, and water vapor partial pressure, $\Delta pH_2O$) is entirely due to oxygen ion permeation through the disc. The gas composition of the output gas was obtained from the $H_2$–$H_2O$ equilibrium condition using the measured oxygen partial pressure. The oxygen flux through the sample ($jO_2$) was determined as:

$$jO_2 = \frac{(\Delta pO_2 + (1/2)\Delta pH_2O) \cdot Q}{A} \quad (1)$$

where $Q$ is the flow rate of the sweep gas and $A$ is the exposed disc area.

In chemical compatibility studies, $Y_{0.8}Ca_{0.2}Cr_{0.85}Ni_{0.15}O_{3\pm\delta}$ powder was mixed with 8 mol% YSZ powder to obtain a 50:50 weight ratio, ball-milled for 24 h and fired in air at 1400 °C for 12 h. The resulting specimen was crushed and the powder was analyzed by XRD.

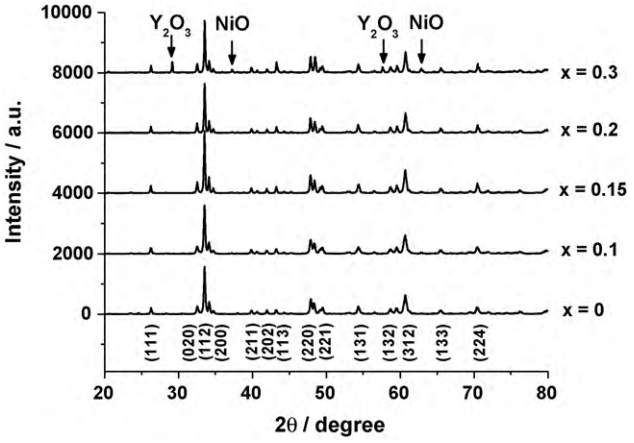


**Fig. 1.** XRD patterns of $Y_{0.8}Ca_{0.2}Cr_{1-x}Ni_xO_{3\pm\delta}$ ($x$ = 0–0.3) powders after calcinations at 1200 °C in air for 2 h.

## 3. Results and discussion

### 3.1. Phase structure and stability

Fig. 1 shows the XRD patterns of $Y_{0.8}Ca_{0.2}Cr_{1-x}Ni_xO_{3\pm\delta}$ ($x$ = 0–0.3) powders after calcination in air. The XRD patterns show the single phase formation of an orthorhombic perovskite structure up to $x$ = 0.15. Secondary phase peaks such as NiO and $Y_2O_3$ were observed at $x \geq 0.2$. Therefore, the substitutional limit of nickel for the formation of a single phase solid solution is between $x$ = 0.15 and 0.20. The phase stability of $Y_{0.8}Ca_{0.2}Cr_{0.85}Ni_{0.15}O_{3\pm\delta}$ after annealing at 800 °C for 12 h in a reducing environment ($pO_2 = 4 \times 10^{-22}$ atm) was confirmed using XRD. XRD patterns indicated no phase change due to the exposure to reducing atmosphere.

Chromite-based perovskite oxides can undergo an orthorhombic-rhombohedral phase transformation which is likely to cause problems during thermal cycling due to nonlinear thermal expansion behavior [14] and loss of mechanical strength [29]. Especially, calcium-doped lanthanum chromite was reported to show a significant degradation in mechanical properties between 300 and 500 °C because of the orthorhombic-rhombohedral phase transition [23,29]. The phase stability of $Y_{0.8}Ca_{0.2}Cr_{0.85}Ni_{0.15}O_{3\pm\delta}$ between 25 and 1200 °C was examined using high temperature XRD, and a single orthorhombic phase was found in the entire temperature range. Therefore, calcium- and nickel-doped yttrium chromite is expected to show better mechanical strength during thermal cycling than calcium-doped lanthanum chromite. Fig. 2 shows the thermal evolution of (1 1 2) and (2 0 0) peaks. Fitting these XRD peaks allowed obtaining the lattice parameters listed in Table 1. The unit cell volume showed a linear increase with temperature as given in Fig. 3, and the

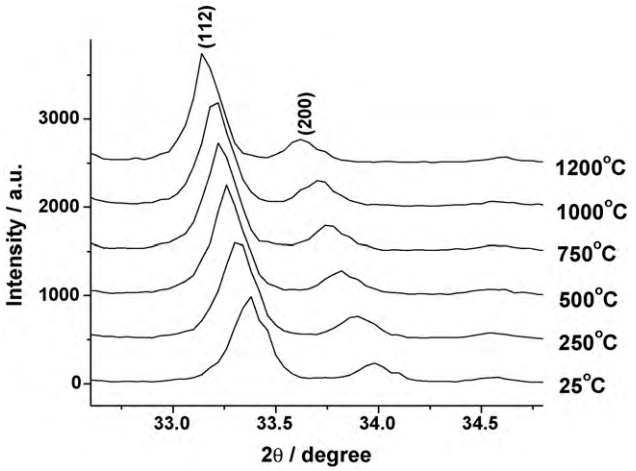


**Fig. 2.** Thermal evolution of selected XRD peaks of $Y_{0.8}Ca_{0.2}Cr_{0.85}Ni_{0.15}O_{3\pm\delta}$ obtained in the temperature range 25–1200 °C in air.

**Table 1**
Unit cell dimension of $Y_{0.8}Ca_{0.2}Cr_{0.85}Ni_{0.15}O_{3\pm\delta}$ calculated at different temperatures.

| Temperature (°C) | *a* (Å) | *b* (Å) | *c* (Å) |
|---|---|---|---|
| 25 | 5.250 | 5.499 | 7.514 |
| 250 | 5.267 | 5.503 | 7.540 |
| 500 | 5.289 | 5.512 | 7.570 |
| 750 | 5.308 | 5.519 | 7.595 |
| 1000 | 5.325 | 5.523 | 7.617 |
| 1100 | 5.334 | 5.524 | 7.627 |
| 1150 | 5.338 | 5.526 | 7.632 |
| 1200 | 5.341 | 5.526 | 7.636 |

thermal expansion coefficient (TEC) of $Y_{0.8}Ca_{0.2}Cr_{0.85}Ni_{0.15}O_{3\pm\delta}$ was estimated to be $11.3 \times 10^{-6}\,K^{-1}$ from the cubic root of the unit cell volume [30]. As reported below, this TEC value was additionally verified with dilatometry measurements.

### 3.2. Sintering behavior

Fig. 4 shows the sintering behavior of green rectangular bars of $Y_{0.8}Ca_{0.2}Cr_{1-x}Ni_xO_{3\pm\delta}$ ($x$ = 0–0.3) between 900 and 1400 °C. Sinterability was remarkably enhanced with nickel doping up to $x$ = 0.15, while further increase in the amount of nickel impaired the sintering properties. Therefore, it appears that nickel doping improves

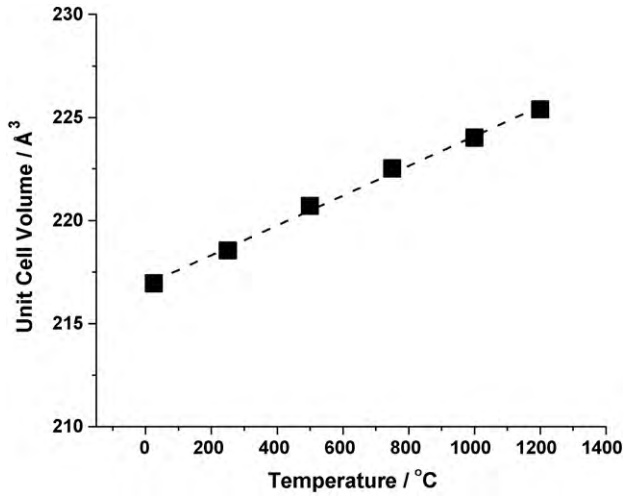


**Fig. 3.** Change of $Y_{0.8}Ca_{0.2}Cr_{0.85}Ni_{0.15}O_{3\pm\delta}$ unit cell volume as a function of temperature between 25 and 1200 °C.

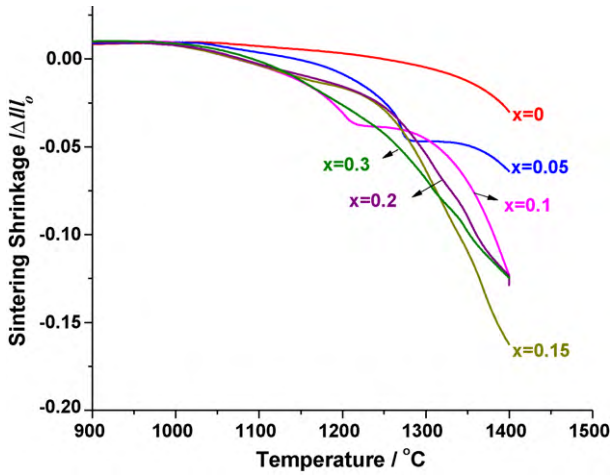


**Fig. 4.** Sintering behavior of $Y_{0.8}Ca_{0.2}Cr_{1-x}Ni_xO_{3\pm\delta}$ ($x$ = 0–0.3) in the 900–1400 °C interval.

the sinterability in a single orthorhombic perovskite phase, while the second phase formation due to the excessive doping suppresses the densification. Chromium-containing oxides are known to be extremely difficult to densify due to volatilization of chromium species and formation of a thin $Cr_2O_3$ layer at the interparticle neck [1,19]. Sinterability of lanthanum chromites has been reported to improve with transition metal doping due to the transient liquid phase formation [31] and/or chromium stabilization resulting in reduced volatilization rate of chromium species [16]. Sinterability of yttrium chromite is considered to be improved by Ni-doping for similar reasons. In Fig. 4, inflection points are observed in the sintering curves between 1200 and 1300 °C for $x$ = 0.05–0.15. Inflections in sintering curves generally suggest a change in the sintering mechanism at that point. Pronounced curvature change in sintering curve is usually an indication of the generation of a liquid phase [32], and further study is required to elucidate the sintering mechanism of this system. The relative densities measured through the Archimedes method showed that ~94% of theoretical density can be obtained for $x$ = 0.15 at 1400 °C while 81% and 65% of theoretical density were observed for the same composition at 1350 and 1300 °C, respectively. Since an acceptable relative density of ceramic interconnect is >94% [33], the present study indicates that adequately dense interconnects can be fabricated by co-firing at ~1400 °C with an optimum amount of Ni dopant in the $Y_{0.8}Ca_{0.2}Cr_{1-x}Ni_xO_3$ system. Fig. 5 shows the SEM images of $Y_{0.8}Ca_{0.2}Cr_{1-x}Ni_xO_{3\pm\delta}$ ($x$ = 0, 0.15 and 0.3) sintered at 1400 °C for 4 h and thermally etched at 1375 °C. The sample without nickel, Fig. 5(a), was highly porous (55% of theoretical density) and the average particle size was ~0.4 μm, which indicates a limited amount of sintering and coarsening of the powder. Open pores significantly decreased and the average grain size increased with nickel doping, Fig. 5(b) and (c). In addition, backscattered electron image and EDS analysis revealed the formation of secondary phases (nickel oxide and yttrium oxide: dark area) at a higher nickel content of 30%, Fig. 5(c), which was consistent with XRD observations (Fig. 1).

### 3.3. Thermal expansion

Fig. 6 shows the TECs of $Y_{0.8}Ca_{0.2}Cr_{1-x}Ni_xO_{3\pm\delta}$ ($x$ = 0–0.3) in air in the 100–900 °C temperature interval measured by dilatometry. There was no indication of non-linear thermal expansion behavior within the measured temperature range, which further confirms the phase stability. TEC increased from $9.7 \times 10^{-6}\,K^{-1}$ to $11.5 \times 10^{-6}\,K^{-1}$ with increasing nickel content from $x$ = 0 to

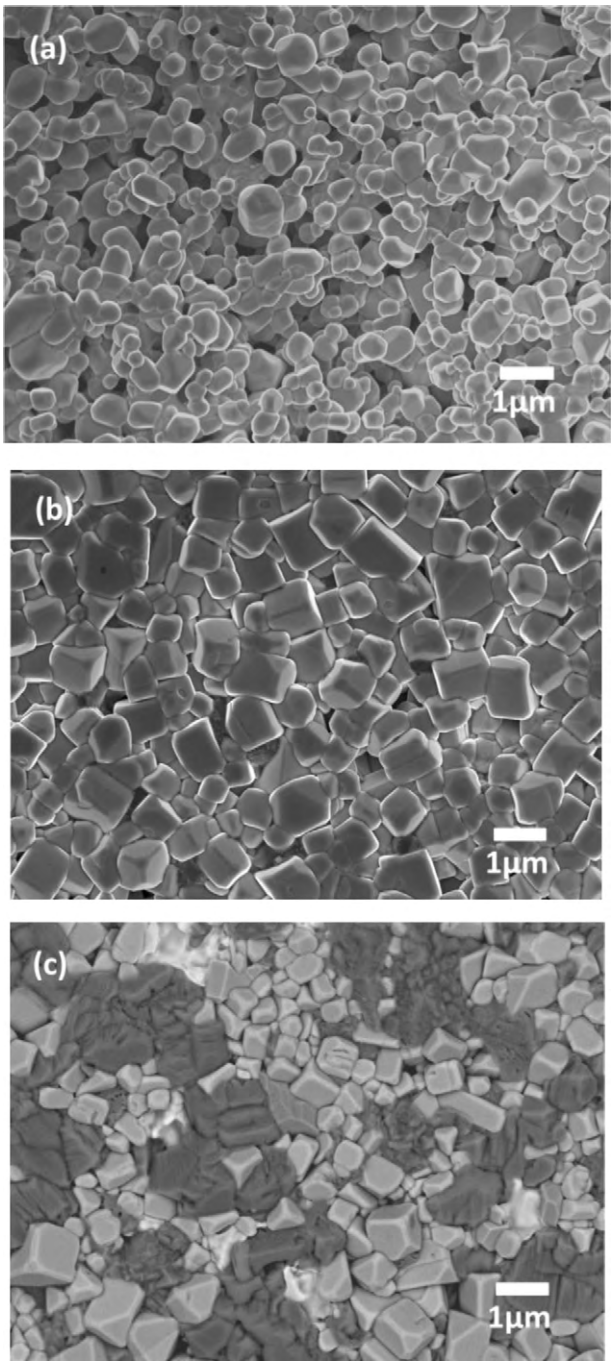


**Fig. 5.** Microstructures of $Y_{0.8}Ca_{0.2}Cr_{1-x}Ni_xO_{3\pm\delta}$ sintered at 1400 °C for 4 h and thermally etched at 1375 °C: (a) $x = 0$, (b) $x = 0.15$, and (c) $x = 0.3$.

0.15, and the results are reasonably consistent with the values estimated by high temperature XRD (Table 1 and Fig. 3). It is important to match the thermal expansions of the cell components in order to minimize the thermal stress in the SOFC stack caused by thermal cycles, and it closely matches that of 8 mol% YSZ ($\sim 10.8 \times 10^{-6}\,K^{-1}$ [34]) when $x$ is between 0.05 and 0.15. Without Ni-doping, the TEC of calcium-doped lanthanum chromite linearly increases with calcium content, and requires more than 30% calcium for the TEC to match that of YSZ [2]. However, chromite-based materials with more than 25% of calcium doping are considered to be less stable due to the secondary phase formation of calcium chromate ($CaCrO_4$) [2,22]. Therefore, it would be advantageous to control TEC of yttrium chromite by adjusting the amount of

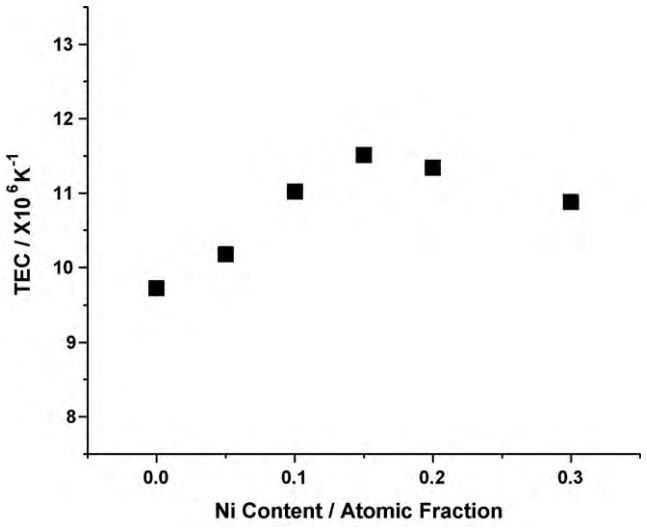


**Fig. 6.** Thermal expansion coefficients (TECs) of $Y_{0.8}Ca_{0.2}Cr_{1-x}Ni_xO_{3\pm\delta}$ ($x = 0$–0.3) in air in the temperature range 100–900 °C.

nickel doping and keep the calcium content below 25% to maintain stability. Further increase in nickel content above $x = 0.2$ is seen to decrease TEC, Fig. 6, likely due to the formation of secondary phases.

### 3.4. Electrical conductivity

The electrical conductivity of $Y_{0.8}Ca_{0.2}Cr_{1-x}Ni_xO_{3\pm\delta}$ ($x = 0$–0.3) was measured in the temperature range 600–900 °C in air as shown in Fig. 7. The electrical conductivity increases with temperature, which indicates a thermally activated conduction mechanism. Nickel doping on the B-site leads to a substantial increase in conductivity, and the maximum conductivity value was obtained for $x = 0.15$. In particular, the conductivity at 900 °C increased from 10.2 S cm$^{-1}$ for $x = 0$ to 34.0 S cm$^{-1}$ for $x = 0.15$. The conductivity of $Y_{0.8}Ca_{0.2}Cr_{0.85}Ni_{0.15}O_{3\pm\delta}$ is higher than that of $La_{0.8}Ca_{0.2}CrO_{3\pm\delta}$ reported by Sakai et al. [35] (~20 S cm$^{-1}$ at 1000 °C). Further increase in nickel content lowered the electrical conductivity, possibly due to the secondary phase formation. It is known that calcium-doped yttrium chromite conducts electricity via the small polaron hopping process [26]. In thermally activated small polaron hopping transport, the number of charge carriers is constant or

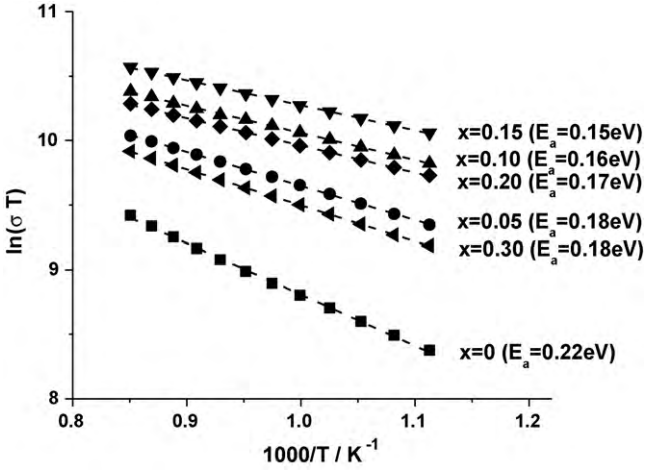


**Fig. 7.** Plot of $\ln(\sigma T)$ versus $1000/T$ for $Y_{0.8}Ca_{0.2}Cr_{1-x}Ni_xO_{3\pm\delta}$ ($x = 0$–0.3) in air in the 600–900 °C temperature interval.

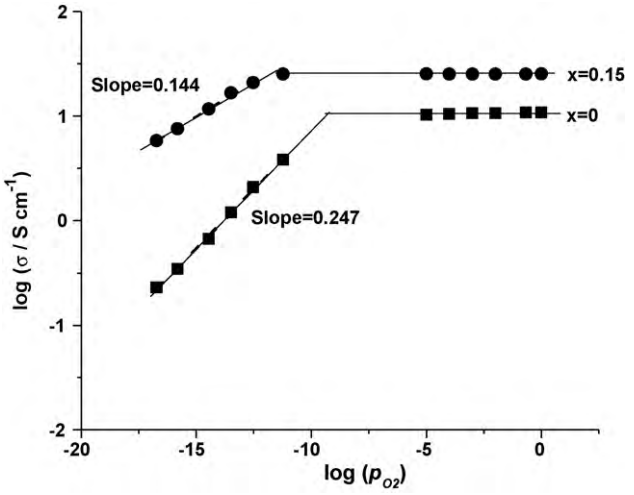


**Fig. 8.** Change in electrical conductivity of $Y_{0.8}Ca_{0.2}Cr_{1-x}Ni_xO_{3\pm\delta}$ ($x = 0$ and 0.15) with oxygen partial pressure and linear fits at 900 °C.

weakly depends on temperature while the mobility is exponentially dependent on temperature [36]. In the adiabatic small polaron hopping conduction, where the carrier is able to jump to an adjacent unoccupied site whenever an atomic displacement favoring the jump occurs, the mobility is expressed as:

$$\mu = (1-x)\left(\frac{ea^2\nu_o}{kT}\right)\ \exp\left(-\frac{E_m}{kT}\right) \quad (2)$$

where $x$ is the fraction of sites occupied, $e$ is the unit charge, $a$ is the distance between the sites, $\nu_o$ is the optical phonon frequency, $E_m$ is the mobility activation energy, and $k$ is the Boltzmann constant. The electrical conductivity is proportional to the product of the carrier density and mobility, and since the charge carrier density is weakly dependent on temperature as shown above, the electrical conductivity, $\sigma$, for adiabatic small polaron hopping can be expressed as [25,37]:

$$\sigma = \frac{A}{T}\ \exp\left(-\frac{E_m}{kT}\right) \quad (3)$$

where $A$ is a charge carrier and material dependent constant. The linear behavior in a plot of $\log(\sigma T)$ versus $1/T$ in Fig. 7 confirms that the adiabatic assumption is valid. The activation energy decreases with nickel doping from 0.22 eV for $x = 0$ to 0.15 eV for $x = 0.15$. Further increase in nickel content increases the activation energy. Obtained values are close to previously reported activation energies of 0.17–0.22 eV for calcium-doped yttrium chromites [21,25]. Nickel doping was reported to lower the activation energy for electric conduction of lanthanum chromites [38], which is also consistent with our findings.

Fig. 8 compares the electrical conductivities of $Y_{0.8}Ca_{0.2}CrO_{3\pm\delta}$ and $Y_{0.8}Ca_{0.2}Cr_{0.85}Ni_{0.15}O_{3\pm\delta}$ as a function of oxygen partial pressure between $10^{-17}$ and 1 atm at 900 °C. The conductivity remains constant throughout the high oxygen partial pressure region, and decreases with decreasing oxygen partial pressure below a critical oxygen partial pressure, which confirms the p-type conduction mechanism. At high oxygen partial pressure, the charge imbalance caused by the introduction of aliovalent dopants is compensated by the formation of holes. Therefore, the number of charge carriers is determined by the amount of doping, and the conductivity is independent of oxygen partial pressure. At low oxygen partial pressure, thermodynamic equilibrium between the defect species and surrounding atmosphere is established through the oxygen exchange reaction which is expressed using Kröger–Vink notation as [39]:

$$O_O^X + 2Cr_{Cr}^{\bullet} \rightarrow V_O^{\bullet\bullet} + 2Cr_{Cr}^X + \frac{1}{2}O_2 \quad (4)$$

Eq. (4) indicates that in reducing atmosphere, loss of lattice oxygen to the atmosphere creates a doubly charged oxygen vacancy and consumes two holes. Therefore, the conductivity develops a strong dependence on oxygen partial pressure as the ionic charge compensation becomes predominant. Improved conductivity with nickel doping at high oxygen partial pressure can be understood as a result of increased charge carrier concentration because most of the nickel ions are divalent and act as acceptor dopants in chromite-based oxides [40]. In the low oxygen partial pressure region, the plot of $\log(\sigma)$ versus $\log(pO_2)$ for $Y_{0.8}Ca_{0.2}CrO_{3\pm\delta}$ shows $pO_2^{1/4}$ dependence. This trend is consistent with the observation of Carini et al. [24], and indicates that ionic charge compensation is predominant and hole concentration is significantly lower than the oxygen vacancy concentration [25,41]. The electrical conductivity of $Y_{0.8}Ca_{0.2}Cr_{0.85}Ni_{0.15}O_{3\pm\delta}$ starts decreasing at a lower oxygen partial pressure ($10^{-12}$ atm) than that of $Y_{0.8}Ca_{0.2}CrO_{3\pm\delta}$ ($10^{-10}$ atm), and the slope of the plot of $\log(\sigma)$ versus $\log(pO_2)$ is 0.144, which indicates that the system does not reach the extreme reducing condition, and both ionic and electronic compensation mechanisms are operative. It was reported that B-site doping of chromite-based perovskite oxides significantly affects oxygen vacancy formation because of the stronger bonding of B–O than A–O [39]. It could be suggested that nickel doping on B-site stabilizes the defect structure of yttrium chromite and suppresses the oxygen vacancy formation in reducing environment, and further studies are required to clarify the mechanisms of defect structure stabilization upon nickel doping. The electrical conductivity of $Y_{0.8}Ca_{0.2}Cr_{0.85}Ni_{0.15}O_{3\pm\delta}$ at 900 °C in reducing atmosphere ($pO_2 \approx 10^{-17}$ atm) was 5.8 S cm$^{-1}$, which is more than an order of magnitude higher than that of $Y_{0.8}Ca_{0.2}CrO_{3\pm\delta}$ (0.2 S cm$^{-1}$).

### 3.5. Oxygen permeation

The electrochemical oxygen permeation through the interconnects can cause significant efficiency loss, especially for SOFC stack designs employing thin interconnects with high surface area because the SOFC interconnects are exposed to a large oxygen chemical potential gradient. Oxygen ionic leak current leads to an electrochemical consumption of fuel and reduction in the energy conversion efficiency. There have been different approaches to investigate the oxygen permeation through the interconnect materials, including the electrical conductivity relaxation method [42], electron blocking electrode method [43,44], oxygen tracer diffusion method [45,46], and electrochemical method employing zirconia oxygen pump [45,46]. Most of these experiments were performed under a homogeneous or small step of oxygen partial pressure, and the estimation of oxygen permeation flux under the large oxygen chemical potential gradient is controversial [42,43,45]. In this study, the SOFC operating condition was simulated by exposing one side of a dense $Y_{0.8}Ca_{0.2}Cr_{0.85}Ni_{0.15}O_{3\pm\delta}$ disc to an oxidizing atmosphere ($pO_2 = 0.21$ atm) and the other side to a reducing atmosphere ($pO_2 = \sim 10^{-20}$ atm). The oxygen permeation flux through the sample was determined by direct measurement of the oxygen partial pressure change in the reducing sweep gas. Fig. 9(a) shows the oxygen flux normalized by the sample thickness (2.5 mm) as a function of temperature. Oxygen flux through the sample was negligible below 600 °C, which verified the gas tightness of the system. It was assumed that the oxygen transport through the sample was diffusion-controlled because the sample was sufficiently thick to ignore the contribution of the surface exchange reaction. Therefore, the oxygen flux through the sample, $j[O_2]$, is determined by the ambipolar conductivity of the sample, and the relationship is

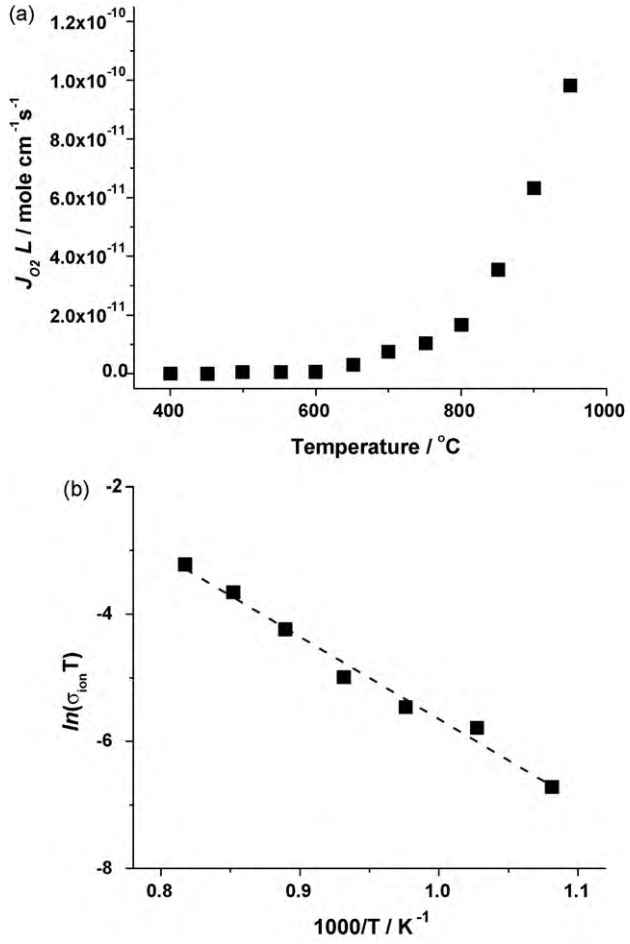


**Fig. 9.** (a) Oxygen flux through $Y_{0.8}Ca_{0.2}Cr_{0.85}Ni_{0.15}O_{3\pm\delta}$ normalized by the sample thickness at different temperatures and (b) Arrhenius plot for the ionic conductivity calculated from the oxygen flux.

given by the Wagner equation as:

$$j[O_2] = -\frac{RT}{4^2F^2L}\int_{\ln p[O_2']}^{\ln p[O_2'']} \frac{\sigma_{el}\sigma_{ion}}{\sigma_{el}+\sigma_{ion}} d\ln p[O_2] \quad (5)$$

where $R$ is the gas constant, $F$ is the Faraday constant, $L$ is the sample thickness, $\sigma_{el}$ is the electronic conductivity, and $\sigma_{ion}$ is the ionic conductivity. If the ionic conductivity is much smaller than the electronic conductivity, the ionic conductivity can be expressed as:

$$\sigma_{ion} = \frac{j[O_2]4^2F^2L}{RT}\ \ln\left(\frac{p[O_2^{(feed)}]}{p[O_2^{(sweep)}]}\right) \quad (6)$$

where $p[O_2^{(feed)}]$ and $p[O_2^{(sweep)}]$ are the oxygen partial pressures of the feed side and sweep side, respectively. Fig. 9(b) shows the temperature dependence of the ionic conductivity calculated by Eq. (6). The relationship between $\ln(\sigma_{ion}T)$ and $1/T$ shows a linear dependence, and the activation energy obtained from the slope is 107 kJ mol$^{-1}$. The leakage current density, $i$, through the interconnect due to oxygen permeation was calculated using the measured oxygen flux according to:

$$i = 4Fj[O_2] \quad (7)$$

The leakage current density between the oxygen partial pressures of $\sim 10^{-20}$ and 0.21 atm at 800 °C was calculated to be 3.2 mA cm$^{-2}$ for a 20 μm thick interconnect. This value is slightly lower than the estimated leakage current of $La_{0.87}Sr_{0.13}Cr_{1.03}O_3$ under the similar condition (3.9 mA cm$^{-2}$) reported by Suzuki et al. [43], and is considered to be acceptable for practical use, because it has been reported that a permeation current density above 0.1 A cm$^{-2}$ can greatly affect the cell efficiency [45].

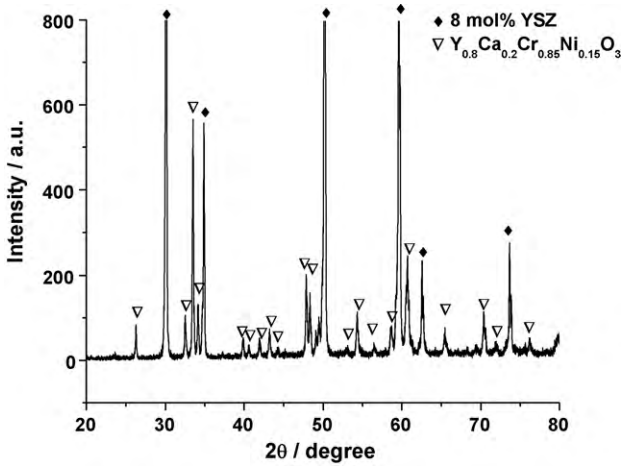


**Fig. 10.** XRD pattern of 50 wt.% of $Y_{0.8}Ca_{0.2}Cr_{0.85}Ni_{0.15}O_{3\pm\delta}$ and 50 wt.% of YSZ mixture after firing in air at 1400 °C for 8 h. No secondary peaks were noticed.

### 3.6. Chemical compatibility

Chemical compatibility of the interconnect material with other cell components is a very important issue because chemical reactions between them can lead to an increase of the cell resistance and/or thermal stresses which cause subsequent cell failure [2]. The chemical compatibility of $Y_{0.8}Ca_{0.2}Cr_{0.85}Ni_{0.15}O_{3\pm\delta}$ with 8 mol% YSZ was studied using XRD analysis. Fig. 10 shows the XRD patterns of mixtures of 50 wt% of $Y_{0.8}Ca_{0.2}Cr_{0.9}Ni_{0.15}O_{3\pm\delta}$ and 50 wt% of 8 mol% YSZ fired at 1400 °C in air for 12 h. The peaks of the composites correspond to those of the individual constituents, $Y_{0.8}Ca_{0.2}Cr_{0.85}Ni_{0.15}O_{3\pm\delta}$ and 8 mol% YSZ. No reaction products (such as $CaZrO_3$ [20]) were observed. Since the conventional Ca-doped $LaCrO_3$ interconnect material can possibly react with zirconia under similar firing conditions and form a highly resistive $La_2Zr_2O_7$ secondary phase [47], lanthanum replacement with yttrium in the A-site is considered to be beneficial in suppressing the undesired reactions.

## 4. Conclusions

In this work, the effect of nickel doping on thermal, structural, and electrical characteristics of calcium-doped yttrium chromite was studied. In the compositions of $Y_{0.8}Ca_{0.2}Cr_{1-x}Ni_xO_{3\pm\delta}$ ($x$ = 0–0.15), nickel doping significantly improved sinterability and electrical conductivity. Secondary phase formation of yttrium oxide and nickel oxide was observed with higher than 20% Ni-doping, which suppressed densification and lowered electrical conductivity. Thermal expansion can be closely matched with that of 8 mol% YSZ through an optimum amount of nickel doping, and oxygen ion leakage current due to exposure to dual atmospheres was shown to be acceptably low using oxygen permeation experiments. A chemical compatibility study between $Y_{0.8}Ca_{0.2}Cr_{0.85}Ni_{0.15}O_{3\pm\delta}$ and YSZ indicated that the formation of detrimental secondary phases is not expected. Based on the results presented in this paper, yttrium chromite with ~20% calcium on A-site and 10–15% nickel on B-site is a promising candidate for interconnect applications in high temperature SOFCs because it offers advantages over the conventional ceramic interconnect materials in terms of the electrical conductivity, sinterability, chemical compatibility and thermal expansion match with the other cell components.

## Acknowledgements

The authors appreciate the high temperature XRD performed by T. Varga, the SEM analysis by A.L. Schemer-Kohrn, and SEM sample preparation by S. Carlson. The work summarized in this paper was funded by the U.S. Department of Energy's Solid-State Energy Conversion Alliance (SECA) Core Technology Program. PNNL is operated by Battelle Memorial Institute for the U.S. Department of Energy under Contract DE-AC06-76RLO 1830.

## References

[1] W.Z. Zhu, S.C. Deevi, Materials Science and Engineering A 348 (2003) 227–243.
[2] J.W. Fergus, Solid State Ionics 171 (2004) 1–15.
[3] T. Kadowaki, T. Shiomitsu, E. Matsuda, H. Nakagawa, H. Tsuneizumi, T. Maruyama, Solid State Ionics 67 (1993) 65–69.
[4] Z. Yang, K.S. Weil, D.M. Paxton, J.W. Stevenson, Journal of The Electrochemical Society 150 (2003) A1188–A1201.
[5] J.W. Fergus, Materials Science and Engineering A 397 (2005) 271–283.
[6] Y. Matsuzaki, I. Yasuda, Solid State Ionics 132 (2000) 271–278.
[7] K. Huang, P.Y. Hou, J.B. Goodenough, Solid State Ionics 129 (2000) 237–250.
[8] Z. Yang, M.S. Walker, P. Singh, J.W. Stevenson, T. Norby, Journal of The Electrochemical Society 151 (2004) B669–B678.
[9] S.C. Paulson, V.I. Birss, Journal of The Electrochemical Society 151 (2004) A1961–A1968.
[10] T.R. Armstrong, J.W. Stevenson, L.R. Pederson, P.E. Raney, Journal of The Electrochemical Society 143 (1996) 2919–2925.
[11] I. Yasuda, M. Hishinuma, Journal of The Electrochemical Society 143 (1996) 1583–1590.
[12] J. Mizusaki, S. Yamauchi, K. Fueki, A. Ishikawa, Solid State Ionics 12 (1984) 119–124.
[13] N. Sakai, H. Yokokawa, T. Horita, K. Yamaji, International Journal of Applied Ceramic Technology 1 (2004) 23–30.
[14] M. Mori, Y. Hiei, T. Yamamoto, Journal of the American Ceramic Society 84 (2001) 781–786.
[15] N. Sakai, T. Kawada, H. Yokokawa, M. Dokiya, T. Iwata, Solid State Ionics 40–41 (1990) 394–397.
[16] S. Hayashi, K. Fukaya, H. Saito, Journal of Materials Science Letters 7 (1988) 457–458.
[17] R. Koc, H.U. Anderson, Journal of Materials Science Letters 11 (1992) 1191–1192.
[18] H.E. Hofer, W.F. Kock, Journal of the Electrochemical Society 140 (1993) 2889–2894.
[19] H. Yokokawa, N. Sakai, T. Kawada, M. Dokiya, Journal of the Electrochemical Society 138 (1991) 1018–1027.
[20] J.D. Carter, C.C. Appel, M. Mogensen, Journal of Solid State Chemistry 122 (1996) 407–415.
[21] S. Wang, B. Lin, Y. Dong, D. Fang, H. Ding, X. Liu, G. Meng, Journal of Power Sources 188 (2009) 483–488.
[22] T.R. Armstrong, J.W. Stevenson, D.E. McCready, S.W. Paulik, P.E. Raney, Solid State Ionics 92 (1996) 213–223.
[23] S.W. Paulik, S. Baskaran, T.R. Armstrong, Journal of Materials Science Letters 18 (1999) 819–822.
[24] G.F. Carini, H.U. Anderson, M.M. Nasrallah, D.M. Sparlin, Journal of Solid State Chemistry 94 (1991) 329–336.
[25] G.F. Carini, H.U. Anderson, D.M. Sparlin, M.M. Nasrallah, Solid State Ionics 49 (1991) 233–243.
[26] W.J. Weber, C.W. Griffin, J.L. Bates, Journal of the American Ceramic Society 70 (1987) 265–270.
[27] K.J. Yoon, J.W. Stevenson, O.A. Marina, Under Review (2010).
[28] L.A. Chick, L.R. Pederson, G.D. Maupin, J.L. Bates, L.E. Thomas, G.J. Exarhos, Materials Letters 10 (1990) 6–12.
[29] S.W. Paulik, S. Baskaran, T.R. Armstrong, Journal of Materials Science 33 (1998) 2397–2404.
[30] V.B. Vert, J.M. Serra, J.L. Jordá, Electrochemistry Communications 12 (2010) 278–281.
[31] R. Koc, H.U. Anderson, Journal of the European Ceramic Society 9 (1992) 285–292.
[32] G.M. Christie, P.H. Middleton, B.C.H. Steele, Journal of the European Ceramic Society 14 (1994) 163–175.
[33] M. Mori, N.M. Sammes, Solid State Ionics 146 (2002) 301–312.
[34] N.Q. Minh, Journal of the American Ceramic Society 76 (1993) 563–588.
[35] N. Sakai, T. Kawada, H. Yokokawa, M. Dokiya, T. Iwata, Journal of Materials Science 25 (1990) 4531–4534.
[36] D.P. Karim, A.T. Aldred, Physical Review B 20 (1979) 2255.
[37] R. Koc, H.U. Anderson, Journal of Materials Science 27 (1992) 5477–5482.
[38] H.E. Hofer, R. Schmidberger, Journal of the Electrochemical Society 141 (1994) 782–786.
[39] S. Onuma, K. Yashiro, S. Miyoshi, A. Kaimai, H. Matsumoto, Y. Nigara, T. Kawada, J. Mizusaki, K. Kawamura, N. Sakai, H. Yokokawa, Solid State Ionics 174 (2004) 287–293.
[40] G.J. Zhang, R. Liu, Y. Yang, Y.Q. Jia, Phys. Status Solidi (A) 160 (1997) 19–27.
[41] R. Koc, H.U. Anderson, Journal of the European Ceramic Society 15 (1995) 867–874.
[42] I. Yasuda, M. Hishinuma, Journal of Solid State Chemistry 115 (1995) 152–157.
[43] M. Suzuki, H. Sasaki, A. Kajimura, Solid State Ionics 96 (1997) 83–88.
[44] V.E.J. van Dieten, J.P. Dekker, J. Schoonman, Solid State Ionics 53–56 (1992) 611–614.
[45] N. Sakai, T. Horita, H. Yokokawa, M. Dokiya, T. Kawada, Solid State Ionics 86–88 (1996) 1273–1278.
[46] T. Kawada, T. Horita, N. Sakai, H. Yokokawa, M. Dokiya, Solid State Ionics 79 (1995) 201–207.
[47] T. Yamamoto, H. Itoh, M. Mori, N. Mori, T. Watanabe, N. Imanishi, Y. Takeda, O. Yamamoto, Journal of Power Sources 61 (1996) 219–222.